Effect of catalytic graphitization on the electrochemical behavior of wood derived carbons for use in supercapacitors

A. Gutiérrez-Pardo, J. Ramírez-Rico*, R. Cabezas-Rodríguez, J. Martínez-Fernández

Departamento Física de la Materia Condensada - ICMS (Universidad de Sevilla-CSIC), Avda. Reina Mercedes S/N, 41012 Seville, Spain.

Abstract

Porous graphitic carbons were successfully obtained from wood precursors through pyrolysis using a transition metal as catalyst. Once the catalyst is removed, the resulting material mimics the microstructure of the wood and presents high surface area, open and interconnected porosity and large pore volume, high crystallinity and good electrical conductivity, making these carbons interesting for electrochemical devices. Carbons obtained were studied as electrodes for supercapacitors in half cell experiments, obtaining high capacitance values in a basic media (up to 133 $F \cdot g^{-1}$ at current densities of 20 $mA \cdot g^{-1}$ and 35 $F \cdot g^{-1}$ at current densities of 1 $A \cdot g^{-1}$). Long-cycling experiments showed excellent stability of the electrodes with no reduction of the initial capacitance values after 1000 cycles in voltammetry.

Keywords: supercapacitors; carbon materials; pyrolysis; graphite; electrochemistry

1 Introduction

Electric double-layer capacitors (EDLCs) have received considerable attention as energy storage/conversion devices because they exhibit high power density, long cycling life, a high charge/discharge capability and are environmentally friendly [1-5]. Supercapacitors are similar in design and manufacture to batteries, but in contrast to them, where the cycle

* corresponding author: [jrr@us.es, Tel. +34 954 550963]

life is limited because of the repeated contraction and expansion of the electrode upon cycling, EDLC lifetime is in principle infinite, as it operates solely on electrostatic surface charge accumulation, without any noticeable performance change [6, 7]. Thus, EDLCs are well suited as backup sources due to their low cost and maintenance-free operation. Supercapacitors have gained considerable interest in different fields such as transportation (electric vehicles), industrial (uninterruptible power sources), digital communications system (cell phones), and others [8].

The capacitance of a supercapacitor is largely dependent on the characteristics of the electrode material. The science and technology of supercapacitors has been reviewed for a number of electrode materials, including carbon, mixed metal oxides, and conducting polymers [9]. More work has been done using porous carbons than with any other material and most of the commercially available devices use carbon electrodes. They have desirable physical and chemical properties, including variety of available forms (powders, fibers, aerogels, composites, monoliths, nanotubes, etc.), ease of processing, controllable porosity, stability in different solutions (from strongly acidic to basic) and ability to perform in a wide range of temperatures [9, 10]. The factors that dictate the selection of carbon materials for electrodes include high surface area and high electrical conductivity, but also interconnected pore structure, controlled pore size matching to that of the electrolyte ions, good wettability towards the electrolyte and the presence of electrochemically stable surface functionalities [11, 12]. The ELDC capacitance arises from the charge separation at the electrode and electrolyte interface, and porous carbonaceous structures can increase the effective contact area between the electrode and electrolyte. The storage charge can be limited in some conventional carbons because they contain an abundant proportion of micropores (pore size < 2nm) that are not easily accessible to ions of the electrolyte. Carbons containing interconnected mesopores (2-50 nm) are desirable for ELDCs electrodes, but meso/micro porosity must exist because if only mesopores are

present in the material the volumetric capacitance decreases due to a lower density of the carbon [13].

Most porous carbon materials have the disadvantage of needing binders or additives which can block part of the porosity of the carbon. The possibility of using activated carbon materials without a binding substance gives an additional benefit from the construction point of view. Monolithic porous carbons with large surface area have long been used as electrode in supercapacitors and demonstrated to be ideal candidates due to their relatively low cost, good electronic conductivity, high surface area and availability [1, 14, 15].

The design of novel structures by mimicking the cellular tissue anatomy of natural biostructures has become a matter of increasing interest [16-18]**.** Recent examples in the field of energy storage include the use of biomass waste such as banana peel [19] or naturally abundant algae [20] as templates for the synthesis of functionalized carbon structures. In the past, we have employed these porous carbon materials that replicate the microstructure of the natural wood as scaffolds towards the synthesis of carbide ceramics [21, 22]. Carbon obtained by pyrolysis of wood presents structural disorder that prevents its graphitization with a subsequent heat treatment; for instance, Pappacena *et al.* showed that wood derived pyrolytic carbon remains essentially amorphous after exposure to temperatures up to 2400ºC in vacuum [23]. For this reason, wood derived carbon is considered *hard* or *non-graphitizing*. However, graphitization can be induced by using a catalyst during pyrolysis, usually a transition metal [24, 25], and this process has been shown to enhance capacitance in carbon materials by both increasing conductivity as well as generating an abundance of mesopores. Recent examples of the use of catalysts to induce graphitization of pyrolytic carbon in the field of energy storage applications include nickel on carbon microspheres [26], MnO_2 catalyzed carbon microspheres [27] or polymer derived (Fe, Co, Ni)-catalyzed carbon monoliths [28].

Here we explore the application of graphitized wood-derived carbons in energy storage applications. This study proposes the use of Fe as catalyst to treat the natural precursor (wood in our case) and obtain the formation of graphite during the pyrolysis process. Afterwards the catalyst is removed to obtain a monolithic, macroporous, partially graphitized carbon material that combines the properties of pyrolysis derived carbons, such as open and interconnected porosity and large pore volume, with the properties of graphite such as high crystallinity and good thermal and electrical conductivity. This paper analyzes the microstructure and the electrochemical behavior of partially graphitized biocarbons processed at different temperatures, and compares them to wood derived pyrolytic carbons obtained without the use of a graphitization catalyst.

2 Experimental

2.1 Materials

Wood-derived carbons were produced from beech (*Fagus silvatica*) precursors. Pieces of wood were cut into blocks with dimensions ca. (15 x 15 x 75) mm^3 and dried in an oven at 100 °C to release adsorbed water from the pores. Iron was chosen as the graphitization catalyst which was prepared into a 3M $FeCl_3$ solution in isopropanol and used to impregnate the wood samples in vacuum for 2 hours to ensure complete filling of the pores. Subsequently, the wood samples were heated until complete drying, evaluated by periodic weight measurements, and stored in a stove until further use.

The pyrolysis process took place in a tube furnace with controlled and constant flow of nitrogen. Pyrolysis was carried out with a ramp rate of 1ºC/min to 500ºC; 5ºC/min to maximum temperature (1000 to 1600ºC), soak time of 30 minutes and 5ºC/min for cooling down to room temperature. This temperature program was chosen to ensure that crack-free carbon monoliths could be obtained.

After pyrolysis, the residual iron was removed by stirring in concentrated HNO_3 (69%, Panreac). The resulting biocarbon monoliths were rinsed and stirred in acetone until neutral pH, and then dried. Samples without catalyst were made to evaluate the effect of graphitization on the electrochemical behavior under similar conditions on treated/untreated carbons.

2.2 Characterization

For a microstructural evaluation of the samples, scanning (SEM, JEOL 6460-LV) and transmission electron microscopy (TEM, Philips CM-200) were used. To prepare samples for TEM, carbon samples were ground, dispersed in ethanol and sonicated for 30 minutes. A drop of this dispersion was deposited on a copper grid with a reticulated amorphous carbon film and allowed to dry.

To determine the thermodynamic characteristics of the graphitization process, thermogravimetric analysis (TGA) and differential scanning calorimetry (DSC) were carried out using a dual beam thermobalance (Thermal Advantage SDT-600) which monitored the weight loss and the heat flow *in-situ* during the pyrolysis, both for treated and untreated wood precursors. Measurements were performed in nitrogen flow using a 20 °C/min heating rate up to 1400ºC.

Residual amounts of hydrogen and nitrogen were determined in a fast combustion furnace using pure oxygen (LECO-CHNS 932), while residual Fe content was measured by ICP-OES (Horiba Ultima 2). Oxygen content was determined by x-ray fluorescence spectroscopy (PANalytical AXIOS).

Samples were studied to determine the effect of the catalytic treatment and the maximum pyrolysis temperature on the degree of graphitization. Crystallinity was determined by X-ray diffraction in a powder diffractometer (A25 D8 Advance, Bruker), and the degree of structural disorder in the carbon structures was evaluated by Raman spectroscopy

(LabRam Jobin Yvon provided with a confocal microscope) with an excitation wavelength of 532 nm, in the spectral region between 1000 and 1800 cm^{-1} which yields the most interesting structural information on carbonaceous materials [29, 30].

The specific surface area of the studied carbon materials was determined by the BET method based on nitrogen adsorption isotherms using a Micromeritics ASAP 2420 Analyzer. Samples previously cut into small pieces to feed into a glass bulb were outgassed at 400ºC for 10 hours and placed in a Dewar vessel to analyze the adsorbed and desorbed amount in the material at 77K in the relative pressure range of P/P_0 = 0-1.

Bulk electrical resistivity was measured at room temperature using the four-terminal sensing method. Carbons were previously cut into bars with dimensions of about (50 x 3 x 3) mm^3, and current intensities from 1 to 100 mA were applied in the extremes of the bars, using a constant intensity power supply (Iso-Tech IPS 3202), measuring the voltage between two fixed points at 15 mm span. The electrical resistance was obtained according to Ohm´s Law (V = IR), and the resistivity was calculated from the resistance using the measured specimen dimensions.

2.3 Evaluation of the electrochemical properties.

Carbon electrodes were prepared as nominal 1 cm^2 slabs with a 1 mm thickness and an approximate mass of 50 mg; electrical connections were performed using Cu wire and silver paste for contacts. The electrochemical measurements of the electrode materials were carried out using a Solartron 1287A potentiostat/galvanostat with a 1260A frequency response analyzer, in a three-electrode setup: wood derived carbon samples were used as working electrodes, an Ag/AgCl electrode was used as a reference and platinum as the counter electrode. The electrolyte in all cases was 1M KOH. Cyclic voltammetry (CV) experiments were performed using scan rates ranging from 1 to 30 $mV \cdot s^{-1}$, at potentials between -1.0 and 0.0 V. Galvanostatic charge/discharge experiments were performed at current densities ranging from 20 to 2000 $mA \cdot g^{-1}$ at a potential window of -

0.8 V. Electrochemical impedance spectroscopy measurements were performed at 10 mV amplitude and 0 V open circuit potential at frequencies in the range 10^{-3}-10^{5} Hz. The cyclic stability of the working electrode was also evaluated for 1000 cycles for graphitized carbons in cyclic voltammetry, at a scan rate of 10 $mV \cdot s^{-1}$.

3 Results and discussion

3.1 Structural characterization.

After impregnation of wood in a $FeCl_3$ solution for 2 hours, a mean dry weight increases of 7 ± 2 % was determined, while geometrical volume remained essentially unchanged. After pyrolysis the precursor retained its original shape, while changes in weight and volume were independent of the pyrolysis temperature. The average weight reduction in the samples was 66 ± 2% and the volume reduction was 68 ± 6%.

Microstructural characterization of the obtained biocarbons was performed using SEM and TEM. Figure 1 shows SEM images for treated carbons pyrolyzed at 1000, 1300 and 1600ºC before and after Fe removal, both using secondary electrons to show the microstructure of the carbon scaffold as well as backscattered electrons to reveal the size and morphology of the Fe particles. The microstructure of the carbon scaffold replicates that of the original wood, consisting of interconnected and aligned channels of a bimodal size distribution. After etching with HNO_3, a soluble salt of iron that eliminates the catalyst is formed and Fe particles are removed from the material. A carbon skeleton which mimics the microstructure of the natural precursor with open and interconnected porosity is thus obtained. Residual Fe content was evaluated to determine the extent of Fe removal during etching, and results are included in Table 1. It was found that residual Fe accounted for less than 0.5 % weight in the case of catalyzed samples and was almost negligible (attributable to oligo-elements present in the wood precursor) in the case of untreated samples. Other residual elements included hydrogen, nitrogen and oxygen (Table 1).

Size and morphology of Fe particles in the carbon scaffold was quantified from SEM measurements, consisting in globular agglomerates in the range of ~1-2 μm. No significant changes in these particles were observed when the peak pyrolysis temperature exceeded the melting point of iron.

Figure 2(a) shows a micrograph obtained by transmission electron microscopy for a treated sample pyrolyzed at 1600 °C, showing Fe particles encapsulated in hollow carbon spheres. The graphitization takes place probably by deposition of turbostratic layers that precipitate from carbon dissolved in the Fe particles. When Fe is removed, hollow and ordered carbon nanostructures remain in the material, as can be seen in Figure 2(b) and will be further discussed below. Highly ordered regions with a plate like morphology and consisting of stacked graphite layers were also detected in samples pyrolyzed at 1600ºC; in Figure 2(c) these plate-like graphitic regions are shown with the associated convergent beam pattern showing individual diffraction spots. Additional evidence of this ordering is the Moiré fringes visible in the micrograph. Finally and for comparison, a TEM micrograph obtained for a sample pyrolyzed without catalyst is shown in Figure 2(d), where none of the previously described features are visible. In contrast with previous works using Ni as a catalyst [25, 31, 32], the mechanism is not dependent of the pyrolysis temperature in the range studied. In the case of wood pyrolyzed at the same temperatures without catalytic treatment, carbon is essentially amorphous, as it was confirmed in the images and SAED patterns in Figure 2(d).

Thermogravimetric analysis (Figure 3) shows an initial weight loss due to the adsorbed water in the carbon up to 150 °C. Decomposition of polysaccharides which are the main components of wood occurs between 200ºC and 400ºC: the hemicellulose is broken up first, followed by cellulose and lignin [33, 34]. In untreated samples no more steps are observed, but in treated samples a third step at about 700ºC is identified. The heat flow during the pyrolysis shows an endothermic curve with a pronounced endothermic peak at

this temperature for the treated sample which does not appear without Fe. This peak is related with the onset of the graphitization process and was confirmed by the presence of a graphite (0002) peak in the XRD pattern of a sample pyrolyzed at 850ºC (not shown). As will be discussed below, this peak is attributed to the formation of pseudo-eutectic liquid droplets in the Fe-C system responsible for the formation of graphitic structures and occurs at temperatures lower than the bulk eutectic temperatures due to size effects [35].

Figure 4 shows XRD patterns of samples studied. Treated carbons present a peak at 2θ = 26.6°, corresponding to (0002) crystal planes of graphite [*pdf 26-1079*] which does not appear in untreated samples which exhibit an essentially amorphous pattern. When the pyrolysis temperature increases, the relative intensity of this graphite peak increases while the peak width decreases. Therefore, the sample pyrolyzed at 1000 °C shows a small and broad peak which indicates the onset of the graphitization, while at 1600 °C the peak is much taller and narrow indicating a higher degree of crystallinity.

In treated samples, we analyzed the specimens before the removal of Fe, obtaining one peak of great intensity at 2θ = 44.8°, and other characteristic peaks *[pdf 06-0696]* which disappear after the acid attack of samples with concentrated HNO_3, confirming the almost complete removal of remaining Fe.

Raman spectra of samples studied are shown in Figure 5. The G band, characteristic for graphitic materials, is located at 1580 cm^{-1} and represents the vibration of the ideal graphite (E_{2g} symmetry). Other bands indicate a disordered graphitic lattice. The D_1 band (1350 cm^{-1}), the most prominent, represents the vibration of graphene layer edges (A_{1g} symmetry), and the D_2 band (1620 cm^{-1}) the vibration of surface graphene layers (E_{2g} symmetry). D_3 band (1500 cm^{-1}) and D_4 band (1150 cm^{-1}) represent the vibration of amorphous regions and local disorder by the presence of ionic impurities [29, 30].

The relationship between the intensity of bands G and D_1 increases in treated samples with the increasing of the pyrolysis temperature and the width to half height (FWHM)

227 decreases in G band, indicating an increase of structural order and a higher amount of
228 graphitic carbon in relation to amorphous carbon, as it was confirmed previously by TEM
229 analysis. In untreated samples, the relative intensity between G and D_1 decreases slightly
230 with temperature.

231 The BET method is a widely used method for the determination of surface area in carbon
232 materials by physical adsorption of gas molecules [36, 37]. All studied samples were
233 previously outgassed at 400ºC for 10 hours. Table 1 summarizes the BET surface area
234 values of different samples studied. Surface area increases strongly in treated samples
235 with respect to untreated samples. Although crystallinity increases with an increasing of
236 the pyrolysis temperature (observed by X-Ray diffraction) the BET surface area values
237 decrease. The highest value of 370 m^2/g is obtained for the treated sample pyrolyzed at
238 1000ºC, the lowest studied temperature. The pore volume increases with the processing
239 temperature: pore dimensions are enlarged, accompanied by a decrease of narrower
240 micropores.

241 The N_2 adsorption isotherms of samples treated with Fe as catalyst and measured after its
242 removal at 77K following degassing at 400ºC are shown in Figure 6 (showing pore size
243 distributions as an insert). Type IV isotherms with hysteresis loops are obtained, initiating
244 at relative pressures $P/P_0 \sim 0.40$, and closing near $P/P_0 = 1$. Mean pore sizes are in the
245 range 6 – 8 nm while median pore sizes are 4 - 5 nm (Table 1), staying in the desirable
246 range for electrochemical storage applications.

247 The electrical resistivity of each sample was determined with a 4-point test fixture,
248 measuring the voltage at applied currents across bar specimens from 1 to 100 mA. Results
249 are shown in Table 1. Resistivity decreases slightly in treated samples respect to untreated
250 samples at the same temperatures, because of increased crystallinity in graphitized
251 samples. The decrease in resistivity with increasing pyrolysis temperature is probably due

to the increase of structural order in the carbon material. Treated samples at 1600ºC show the smallest electrical resistivity at ambient temperature among all of the samples studied.

3.2 Catalytic mechanism

The complex process of catalytic graphitization by transition metals is not completely understood yet, despite intense research activity [35, 38, 39]. The most widely accepted mechanism involves the formation of near eutectic liquid droplets of Fe_xC_y, the exact composition of which is still being debated but suggested to be around 50% atom., which is an anomalously supersaturated solution [39, 40]. These droplets dissolve amorphous domains from the carbon matrix, which precipitate as more ordered graphitic structures due to the associated reduction in free energy, as depicted schematically in Figure 7(a). In this manner, these droplets can tunnel through the carbon matrix as has been observed in *in-situ* TEM experiments ([39] and supplementary material in [35]), giving the microstructures often found in (Fe, Co, Ni) –catalyzed graphitized carbon [24, 28, 31, 38, 41-44]. If these droplets are rapidly cooled by quenching, Fe_3C particles are left which can be detected by x-ray diffraction or other techniques [35] however if the system is cooled slowly the droplets decompose into Fe nanoparticles surrounded by a hollow graphitic structure such as those observed under the TEM in this work (Figure 2 and Figure 7(b)) [45]. Surprisingly, the formation of these liquid droplets occurs at temperatures much lower than those predicted by the bulk Fe-C phase diagram (~ 700ºC as observed in Figure 3 vs. ~1130 ºC of the Fe-C eutectic) [35] which has been attributed to size effects as well as the initial state of the carbon [46]. Ongoing debate regarding this mechanism at the time of writing focuses mainly on the exact composition of these droplets [40] and the mechanism responsible for the low melting temperature, although some authors have found that oxide nanoparticles can catalyze graphitization and carbon nanotube growth without prior carbothermal reduction [47].

3.3 Electrochemical behavior

The electrochemical study of biocarbons was carried out using galvanostatic charge/discharge cycling, electrochemical impedance spectroscopy and cyclic voltammetry.

Figure 8(left) shows charge/discharge curves for Fe-treated carbon scaffolds pyrolyzed at different temperatures and tested at current densities of 20 and 200 $mA \cdot g^{-1}$ (top and bottom, respectively), while Figure 8(right) shows their electrochemical impedance spectra. Galvanostatic charge discharge show essentially triangular shape, characteristic of a charge storage mechanism through formation of an electrical double layer, with the associated *iR* drop being more pronounced in the case of carbon pyrolyzed at 1000 ºC. The obtained electrochemical spectra is characteristic of porous electrodes exhibiting double layer capacitance with frequency dispersion, evidenced in the deviation from verticality of the capacitive (low frequency) branches [48-52]. This deviation is more pronounced for the samples pyrolyzed at 1300 and 1600 ºC suggesting that the availability/size of pores in the samples pyrolyzed at 1000 ºC, as well as surface roughness, reduces capacitance dispersion [53, 54]. This contrasts with the series resistance, determined from the real axis intercept of the spectra, which is higher for the sample pyrolyzed at the lowest temperature in accordance to bulk conductivity measurements as well as galvanostatic charge-discharge curve. Results suggest that there is a trade-off between sample crystallinity (and thus conductivity) and surface and texture characteristics that determine final sample conductivity. Electrochemical impedance curves were fitted using the De Levie model [55] using a constant phase element [53, 54, 56], obtaining frequency dispersion parameters of $\gamma = 0.85$, 0.75 and 0.74 for samples pyrolyzed at 1000ºC, 1300ºC and 1600 ºC respectively (a value of $\gamma = 1$ being the case of an ideal porous electrode with no frequency dispersion), confirming that the best performance is achieved at the lowest pyrolysis temperature used in this work.

Figure 9(a-c) shows cyclic voltammograms at different scan rates for treated samples pyrolyzed at 1000, 1300 and 1600ºC. The shape of the curves appears close to rectangular, consistent with previous results and suggesting an EDLC mechanism. The specific capacitance ($F \cdot g^{-1}$) of the carbon as electrode was calculated from integration of the CV curves. Table 1 summarizes the values of specific capacitances of samples studied.

Treated carbons show a greater capacitance than untreated carbons, as it can be observed in Figure 9(d), indicating a strong improvement in the specific capacitance with the graphitization treatment, due to the enhancement in surface areas in the structure of carbons. Figure 9(e) shows the variation of specific capacitance with power density in all samples studied, and contains capacitance data obtained in both GCD and CV experiments. The specific capacitance of the treated-Fe carbon pyrolyzed at 1000ºC reaches 95 $F \cdot g^{-1}$ at a scan rate of 1 $mV \cdot s^{-1}$. This value decreases to 40 $F \cdot g^{-1}$ when the scan rate is increased from 1 to 30 $mV \cdot s^{-1}$, maybe due to that some parts of the surface of the electrode being inaccessible at rapid charging-discharging rates [11]. In static charge-discharge experiments maximum capacitances at 20 $mA \cdot g^{-1}$ for treated samples were 133 $F \cdot g^{-1}$ (1000 ºC), 34 $F \cdot g^{-1}$ (1300 ºC) and 24 $F \cdot g^{-1}$ (1600 ºC).

Since high cycling stability is essential for such devices, a study of the long cycling life of the material is crucial for its practical application in supercapacitors. A cycling life test over 1000 cycles for Fe-treated carbon electrodes pyrolyzed at 1000ºC was carried out. The capacitance retention as a function of cycle number is showed in Figure 9(f), demonstrating that the material exhibits excellent cycling stability.

While the measured capacitance might not seem impressive, it is important to keep in mind that the mass used for normalization is the total electrode mass, and not the mass of active material as usually reported by other authors. While per unit mass of active material wood-derived carbon might have a lower capacitance than other materials, in

practical applications the total assembly mass, including binders, current collectors and other additives is important for final performance.

4 Conclusions

The use of iron as catalyst has been successful in obtaining graphitic carbons by pyrolysis, a method that usually produces hard, non graphitizable carbons. A mechanism involving growth of graphitic layers around Fe particles, leaving cavities of partially ordered carbon when Fe is removed is observed by electron microscopy in the range of temperatures studied. The degree of crystallinity increases with the pyrolysis temperature. However, graphitization leads to a higher increase in surface area at the lowest pyrolysis temperatures. The CV studies show great capacitive behavior for graphitized carbons: a strong improvement in specific capacitances with respect to untreated carbons and excellent cycling stability. The graphitized carbon facilitates the electrons transport during the processes of charging and discharging because of its conductivity, surface area and mesoporosity. The specific capacitance values obtained at the slowest scan rates is believed to be closest to that of optimum utilization of the material as electrode, showing better results for the lowest temperature which is related to the specific surface areas. A maximum specific capacitance of 133 $F \cdot g^{-1}$ was observed in galvanostatic charge/discharge experiments, a promising value for a binderless monolithic material.

Acknowledgements.

This work was supported by the Junta de Andalucía under grant No. P09-TEP-5152. Electron microscopy, x-ray diffraction and fluorescence, N_2 adsorption and elemental analysis measurements were performed at the CITIUS central services of the University of Seville. Raman scattering measurements were performed at the ICMS (University of Seville-CSIC). A. Gutiérrez-Pardo is grateful to the Junta de Andalucía for a predoctoral grant.

Figure Captions

Figure 1. SEM micrographs of carbon samples pyrolyzed at 1000, 1300 and 1600 ºC after impregnation with Fe, taken before (left) and after (right) removal of Fe by acid washing.

Figure 2. TEM images for carbons pyrolized at 1600ºC. A) Treated with Fe before its removal, where Fe particles are surrounded by a graphitic structure; b) after removal of Fe, leaving partially ordered hollow carbon nanostructures (marked by arrows); c) detail showing plate like graphitic regions and associated electron diffraction pattern; d) without Fe impregnation, carbon obtained is essentially amorphous.

Figure 3. Weight loss and derivative weight loss (top) and heat flow (bottom) versus temperature during pyrolysis of wood, with (red line) and without impregnation with $FeCl_3$ (black line). The weight loss shows a step of about 718ºC for the impregnated sample which does not appear without Fe. The heat flow also shows a pronounced endothermic peak in the curve at this temperature.

Figure 4. X-ray diffraction patterns for carbon materials pyrolyzed at different temperatures, with or withouth a Fe catalyst.

Figure 5. Raman spectra for samples pyrolyzed in the absence (top) and in the presence (bottom) of catalyst.

Figure 6. N_2 sorption isotherms of samples treated with Fe as catalyst at different peak pyrolysis temperatures (inset – pore size desorption distribution).

Figure 7. Schematic of the catalytic mechanism responsible for the formation of partially graphitized carbon. (A) Formation of Fe_xC_y droplets and growth of graphitic structures by solution-precipitation. (B) Decomposition of Fe_xC_y into Fe nanoparticles surrounded by a graphitic shell.

Figure 8. Electrochemical testing results. Left: galvanostatic charge/discharge cycles at 20 mA/g (top) and 200 mA/g (bottom) for Fe-treated carbon samples pyrolyzed at different peak temperatures. Right: EIS of Fe-treated carbon samples at different pyrolysis temperatures. Equivalent series resistance has been substracted to all spectra for ease of comparison.

Figure 9. (a-d) CV curves of carbons treated with Fe, at different scan rates, from 5 to 30 mV/s, made at peak pyrolysis temperatures of (a) 1000, (b) 1300 and (c) 1600ºC. (d) CV curves of carbons treated and untreated with Fe, at a scan rate of 10 mV/s. e) Ragone-type plot showing specific capacitances measured at different power densities, measured using both voltammetric and amperometric tests. F) Capacitance retention of carbon monoliths obtained from Fe-treated wood at 1000ºC as a function of cycle number.

References

[1] M.C. Liu, L.B. Kong, P. Zhang, Y.C. Luo, L. Kang, Electrochim Acta, 60 (2012) 443-448.

[2] G.P. Wang, L. Zhang, J.J. Zhang, Chem Soc Rev, 41 (2012) 797-828.

[3] C. Peng, X.B. Yan, R.T. Wang, J.W. Lang, Y.J. Ou, Q.J. Xue, Electrochim Acta, 87 (2013) 401-408.

[4] B.L. Hu, X.Y. Qin, A.M. Asiri, K.A. Alamry, A.O. Al-Youbi, X.P. Sun, Electrochim Acta, 100 (2013) 24-28.

[5] X.Y. Zhang, X.Y. Wang, L.L. Jiang, H. Wu, C. Wu, J.C. Su, J Power Sources, 216 (2012) 290-296.

[6] A.S. Arico, P. Bruce, B. Scrosati, J.M. Tarascon, W. Van Schalkwijk, Nat Mater, 4 (2005) 366-377.

[7] Y.G. Guo, J.S. Hu, L.J. Wan, Adv Mater, 20 (2008) 2878-2887.

[8] P. Kossyrev, J Power Sources, 201 (2012) 347-352.

[9] A. Burke, J Power Sources, 91 (2000) 37-50.

[10] S.L. Candelaria, Y.Y. Shao, W. Zhou, X.L. Li, J. Xiao, J.G. Zhang, Y. Wang, J. Liu, J.H. Li, G.Z. Cao, Nano Energy, 1 (2012) 195-220.

[11] A.G. Pandolfo, A.F. Hollenkamp, J Power Sources, 157 (2006) 11-27.

[12] L.L. Zhang, X.S. Zhao, Chem Soc Rev, 38 (2009) 2520-2531.

[13] A.B. Fuertes, G. Lota, T.A. Centeno, E. Frackowiak, Electrochim Acta, 50 (2005) 2799-2805.

[14] E. Frackowiak, F. Beguin, Carbon, 39 (2001) 937-950.

[15] V. Ruiz, C. Blanco, R. Santamaria, J.M. Ramos-Fernandez, M. Martinez-Escandell, A. Sepulveda-Escribano, F. Rodriguez-Reinoso, Carbon, 47 (2009) 195-200.

[16] P. Greil, T. Lifka, A. Kaindl, J Eur Ceram Soc, 18 (1998) 1961-1973.

[17] P. Greil, J Eur Ceram Soc, 21 (2001) 105-118.

[18] Z. Schnepp, W. Yang, M. Antonietti, C. Giordano, Angew Chem Int Edit, 49 (2010) 6564-6566.

[19] Y.K. Lv, L.H. Gan, M.X. Liu, W. Xiong, Z.J. Xu, D.Z. Zhu, D.S. Wright, J Power Sources, 209 (2012) 152-157.

[20] Y. Gao, W.L. Zhang, Q.Y. Yue, B.Y. Gao, Y.Y. Sun, J.J. Kong, P. Zhao, J Power Sources, 270 (2014) 403-410.

[21] J.M. Fernandez, A. Munoz, A.R.D. Lopez, F.M.V. Feria, A. Dominguez-Rodriguez, M. Singh, Acta Mater, 51 (2003) 3259-3275.

[22] J. Martinez-Fernandez, F. Valera-Feria, M. Singh, Scripta Mater, 43 (2000) 813-818.

[23] K.E. Pappacena, S.P. Gentry, T.E. Wilkes, M.T. Johnson, S. Xie, A. Davis, K.T. Faber, J Eur Ceram Soc, 29 (2009) 3069-3077.

[24] A. Oya, H. Marsh, J Mater Sci, 17 (1982) 309-322.

[25] M.T. Johnson, K.T. Faber, J Mater Res, 26 (2011) 18-25.

[26] M.X. Liu, L.H. Gan, W. Xiong, F.Q. Zhao, X.Z. Fan, D.Z. Zhu, Z.J. Xu, Z.X. Hao, L.W. Chen, Energ Fuel, 27 (2013) 1168-1173.

[27] M.X. Liu, L.H. Gan, W. Xiong, Z.J. Xu, D.Z. Zhu, L.W. Chen, J Mater Chem A, 2 (2014) 2555-2562.

[28] M. Sevilla, A.B. Fuertes, Carbon, 56 (2013) 155-166.

[29] Y.B. Cai, Y. Hu, L. Song, S.Y. Xuan, Y. Zhang, Z.Y. Chen, W.C. Fan, Polym Degrad Stabil, 92 (2007) 490-496.

[30] A. Sadezky, H. Muckenhuber, H. Grothe, R. Niessner, U. Poschl, Carbon, 43 (2005) 1731-1742.

[31] A. Gutierrez-Pardo, J. Ramirez-Rico, A.R. de Arellano-Lopez, J. Martinez-Fernandez, Journal of Materials Science, DOI: 10.1007/s10853-014-8477-8 (2014) In Press.

[32] Y. Kodama, K. Sato, K. Suzuki, Y. Saito, T. Suzuki, T.J. Konno, Carbon, 50 (2012) 3486-3496.

[33] C.E. Byrne, D.C. Nagle, Carbon, 35 (1997) 267-273.

[34] C.E. Byrne, D.C. Nagle, Carbon, 35 (1997) 259-266.

[35] S. Glatzel, Z. Schnepp, C. Giordano, Angew Chem Int Edit, 52 (2013) 2355-2358.

[36] M. Armandi, B. Bonelli, K. Cho, R. Ryoo, E. Garrone, Int J Hydrogen Energ, 36 (2011) 7937-7943.

[37] K.S.W. Sing, Carbon, 32 (1994) 1311-1317.

[38] H. Marsh, D. Crawford, D.W. Taylor, Carbon, 21 (1983) 81-87.

[39] O.P. Krivoruchko, V.I. Zaikovskii, Mendeleev Commun, (1998) 97-100.

[40] X.F. Feng, S.W. Chee, R. Sharma, K. Liu, X. Xie, Q.Q. Li, S.S. Fan, K.L. Jiang, Nano Res, 4 (2011) 767-779.

[41] M. Sevilla, A.B. Fuertes, Carbon, 44 (2006) 468-474.

[42] M. Sevilla, C. Sanchis, T. Valdes-Solis, E. Morallon, A.B. Fuertes, J Phys Chem C, 111 (2007) 9749-9756.

[43] M. Sevilla, C. Sanchis, T. Valdes-Solis, E. Morallon, A.B. Fuertes, Electrochim Acta, 54 (2009) 2234-2238.

[44] M. Sevilla, A.B. Fuertes, Chem Phys Lett, 490 (2010) 63-68.

[45] J.P. Huo, H.H. Song, X.H. Chen, S.Q. Zhao, C.M. Xu, Mater Chem Phys, 101 (2007) 221-227.

[46] M. Yudasaka, K. Tasaka, R. Kikuchi, Y. Ohki, S. Yoshimura, E. Ota, J Appl Phys, 81 (1997) 7623-7629.

[47] S.A. Steiner, T.F. Baumann, B.C. Bayer, R. Blume, M.A. Worsley, W.J. MoberlyChan, E.L. Shaw, R. Schlogl, A.J. Hart, S. Hofmann, B.L. Wardle, J Am Chem Soc, 131 (2009) 12144-12154.

[48] T. Pajkossy, J Electroanal Chem, 364 (1994) 111-125.

[49] G. Paasch, K. Micka, P. Gersdorf, Electrochim Acta, 38 (1993) 2653-2662.

[50] I.D. Raistrick, Electrochim Acta, 35 (1990) 1579-1586.

[51] O. Bohlen, J. Kowal, D.U. Sauer, J Power Sources, 173 (2007) 626-632.

[52] O. Bohlen, J. Kowal, D.U. Sauer, J Power Sources, 172 (2007) 468-475.

[53] J. Bisquert, G. Garcia-Belmonte, F. Fabregat-Santiago, N.S. Ferriols, P. Bogdanoff, E.C. Pereira, J Phys Chem B, 104 (2000) 2287-2298.

[54] J. Bisquert, G. Garcia-Belmonte, F. Fabregat-Santiago, A. Compte, Electrochem Commun, 1 (1999) 429-435.

[55] R. de Levie, in: P. Delahay (Ed.) Advances in Electrochemistry and Electrochemical Engineering, Wiley Interscience, New York, 1967, pp. 329.

[56] J.A. Rodríguez, M. Fernández Garcia, Synthesis, properties, and applications of oxide nanomaterials, Wiley-Interscience, Hoboken, N.J., 2007.

475 ## Tables

476 Table 1. Most relevant results included in this work.

	Fe-treated carbon			Untreated carbon		
	1000ºC	1300ºC	1600ºC	1000ºC	1300ºC	1600ºC
Maximum capacitance at 1 mV/s ($F \cdot g^{-1}$)	95	33	23	16	3.5	3.1
Maximum capacitance at 10 mV/s ($F \cdot g^{-1}$)	67	21	19	3.8	2.8	1.12
Maximum capacitance at 20 $mA \cdot g^{-1}$ ($F \cdot g^{-1}$)	133	34	24	-	-	-
Maximum capacitance at 1 $A \cdot g^{-1}$ ($F \cdot g^{-1}$)	35	8	5	-	-	-
Electrical resistivity (10^{-4} Ω m)	2.2	0.8	0.6	4.8	3.5	1.9
Equivalent Series Resistance (Ω)	3.0	1.9	2.0	-	-	-
BET surface area ($m^2 \cdot g^{-1}$)	370.2	217.4	167.2	2.1	1.7	1.5
Mean BET pore width (nm)	2.6	3.6	3.6			
BET pore volume ($cm^3 \cdot g^{-1}$)	0.24	0.22	0.15			
Residual hydrogen content (wt. %)	1.25			0.50		
Residual nitrogen content (wt. %)	0.48			0.36		
Residual iron content (wt. %)	0.38			$9 \cdot 10^{-3}$		
Residual oxygen content (wt. %)	4.79			3.48		

477

478

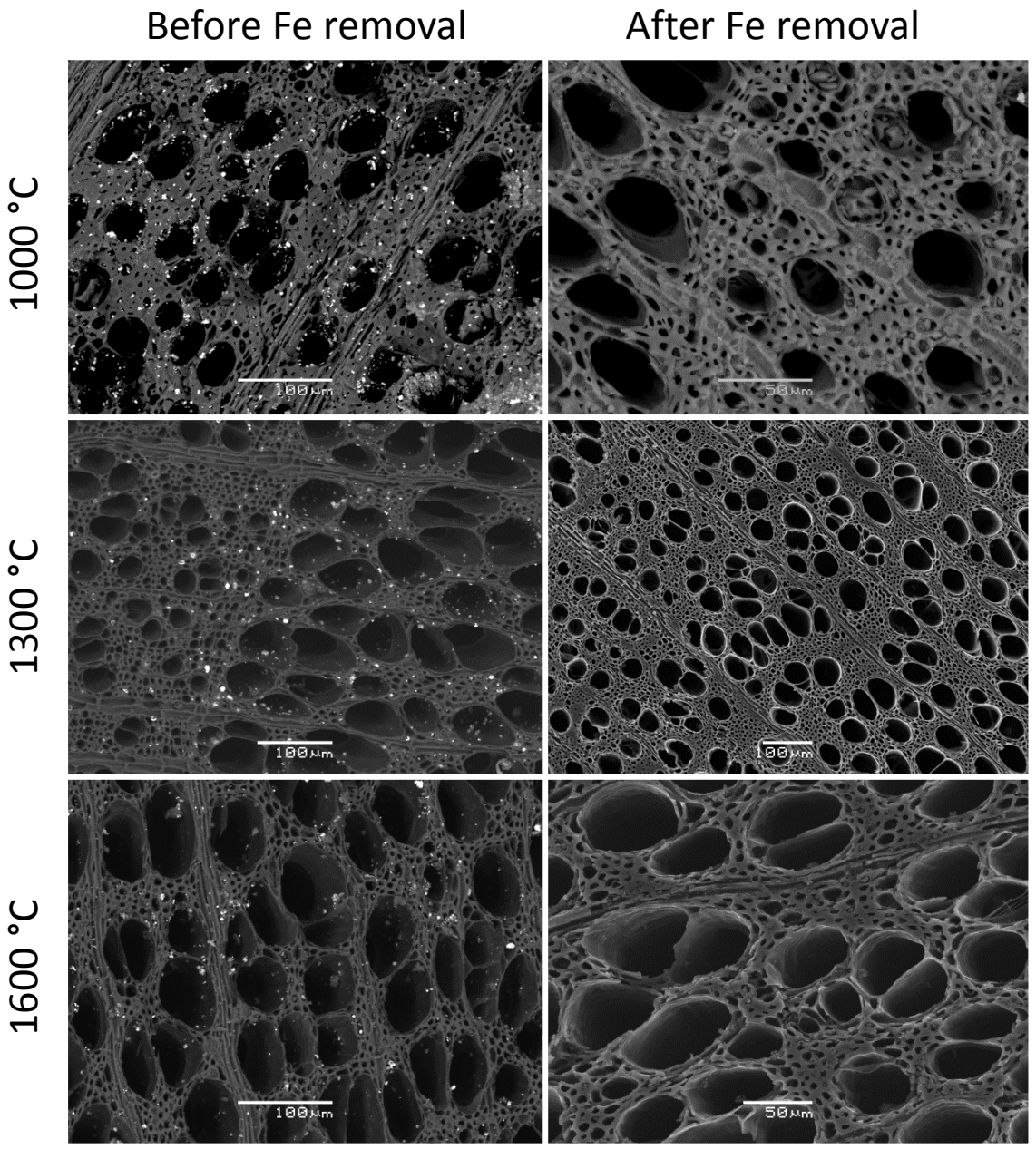
Before Fe removal
After Fe removal
1000 °C
1300 °C
1600 °C
100µm
50µm
100µm
100µm
100µm
50µm

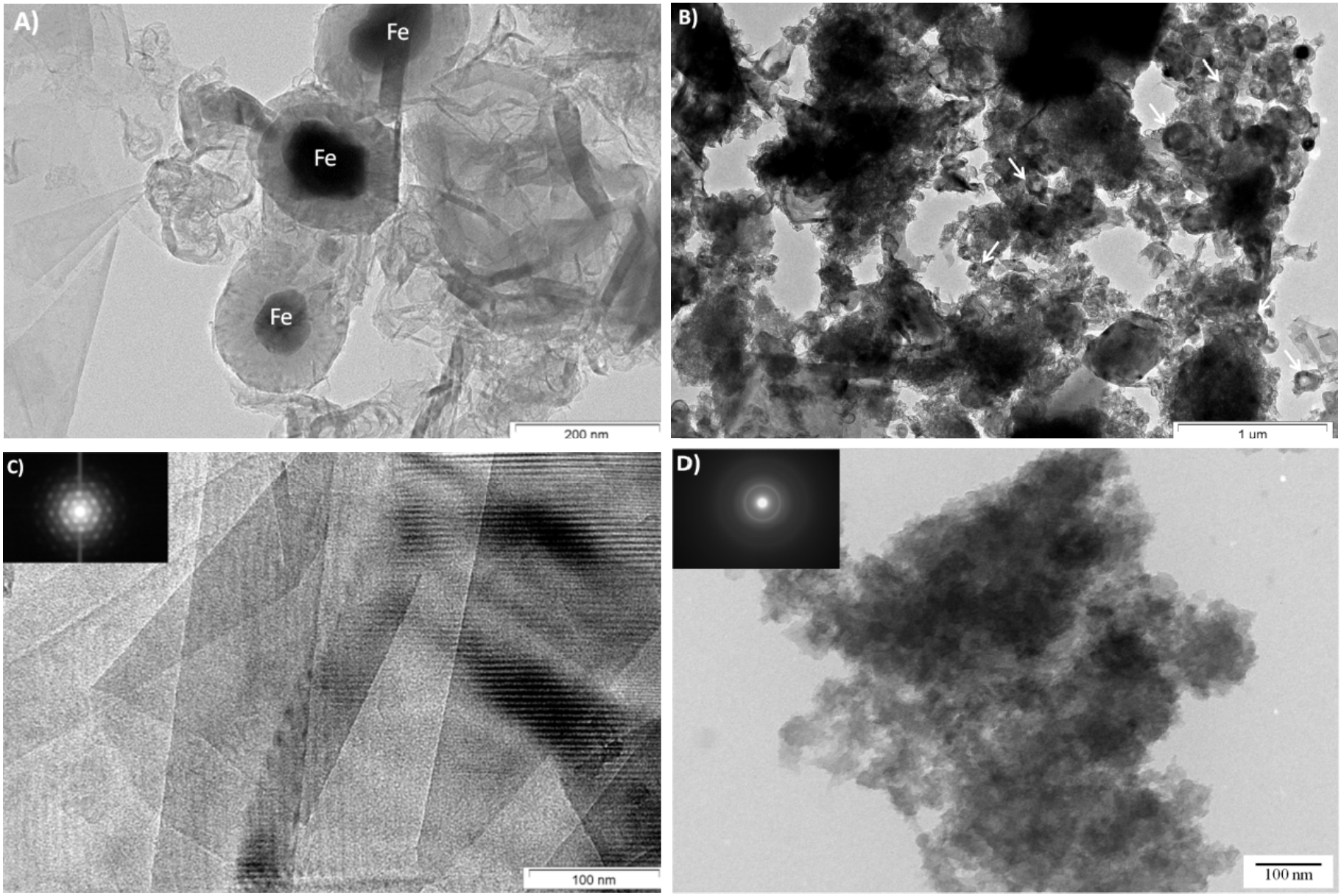
A)
Fe
Fe
Fe
200 nm
B)
1 um
C)
100 nm
D)
100 nm

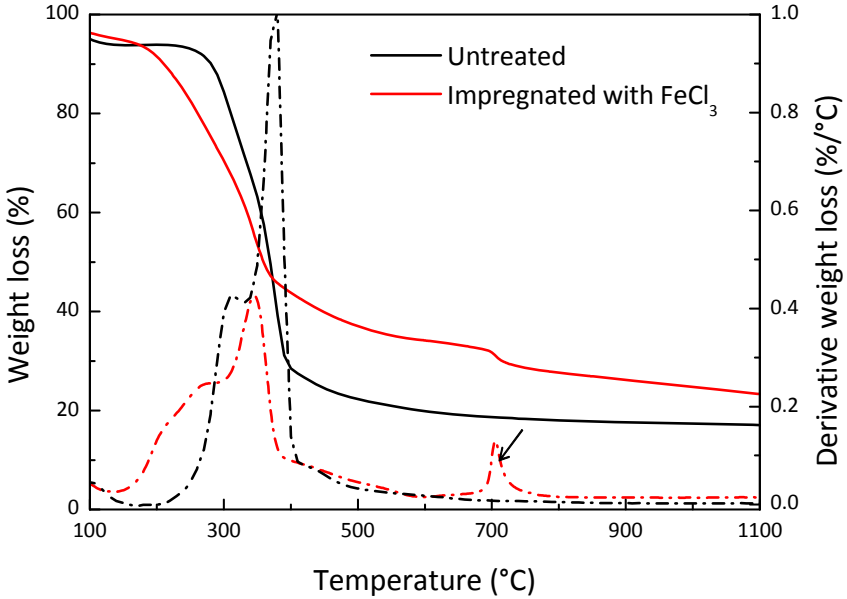
Untreated
Impregnated with FeCl3
Weight loss (%)
Derivative weight loss (%/°C)
Temperature (°C)
100
80
60
40
20
0
1.0
0.8
0.6
0.4
0.2
0.0
100
300
500
700
900
1100

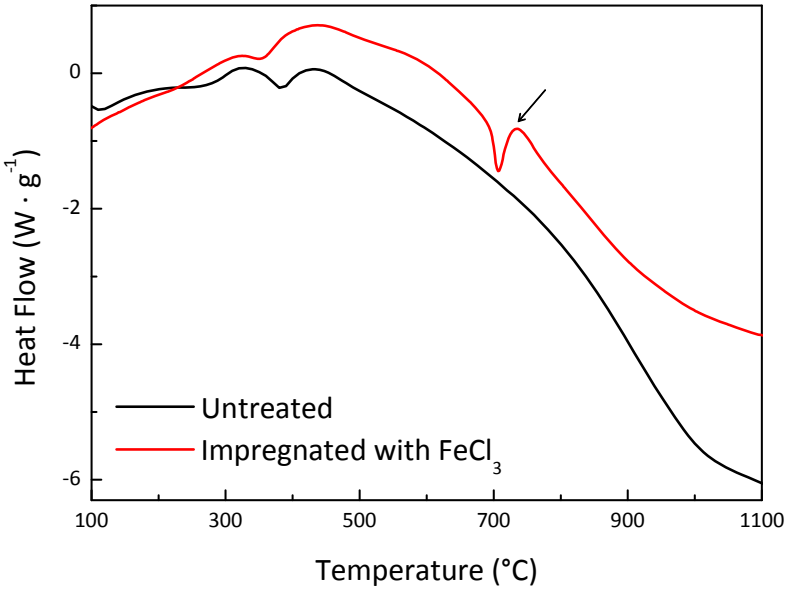
Heat Flow (W · g-1)
Untreated
Impregnated with FeCl3
Temperature (°C)
0
-2
-4
-6
100
300
500
700
900
1100

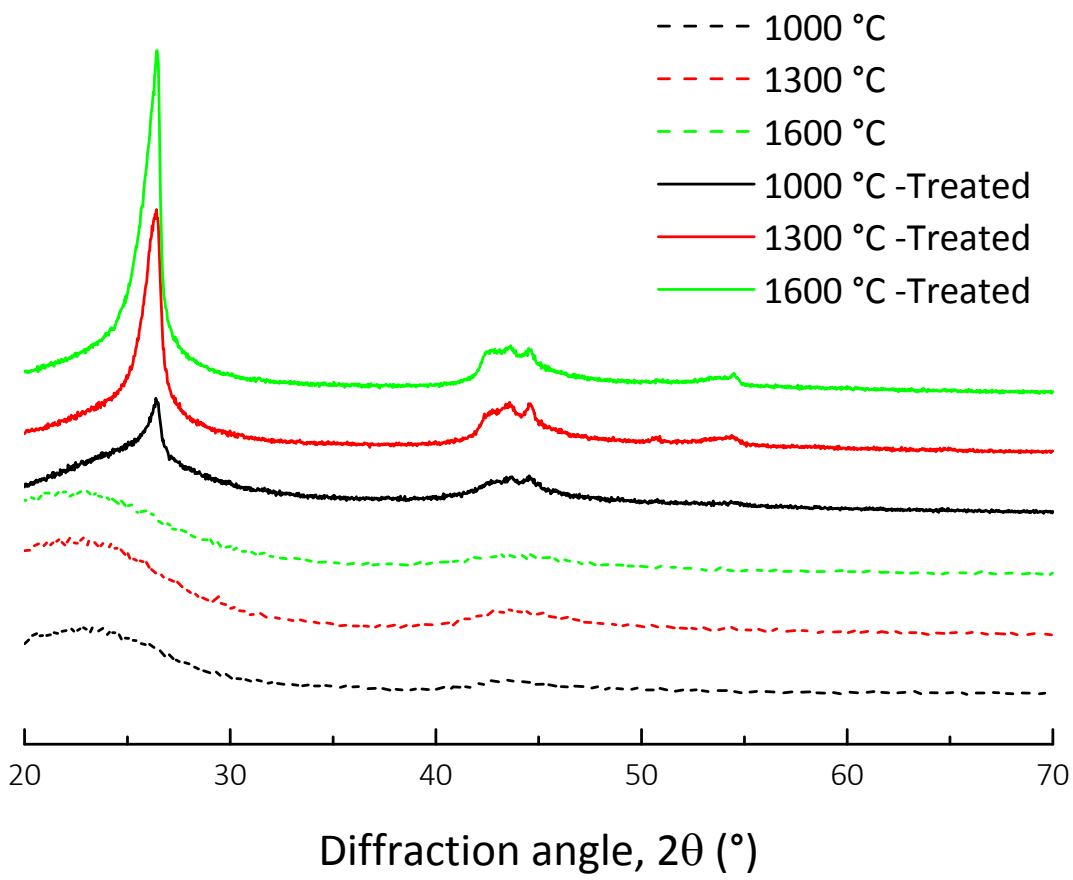
1000 °C
1300 °C
1600 °C
1000 °C -Treated
1300 °C -Treated
1600 °C -Treated
20
30
40
50
60
70
Diffraction angle, 2θ (°)

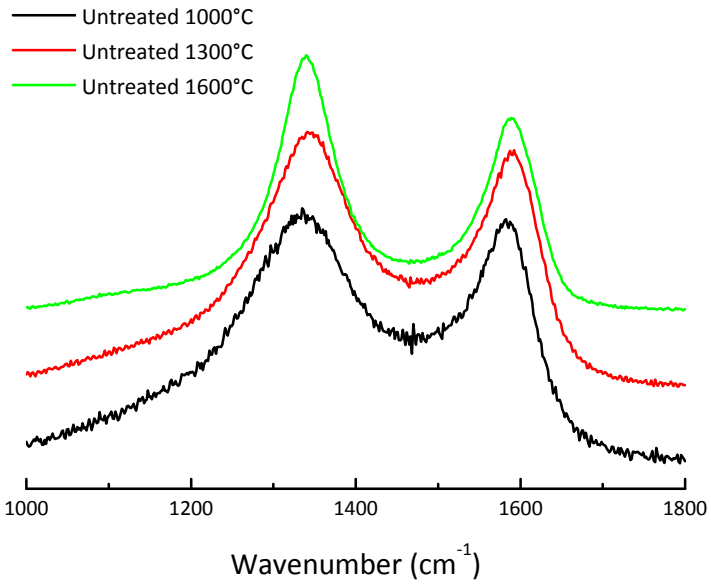
Untreated 1000°C
Untreated 1300°C
Untreated 1600°C
1000
1200
1400
1600
1800
Wavenumber (cm-1)

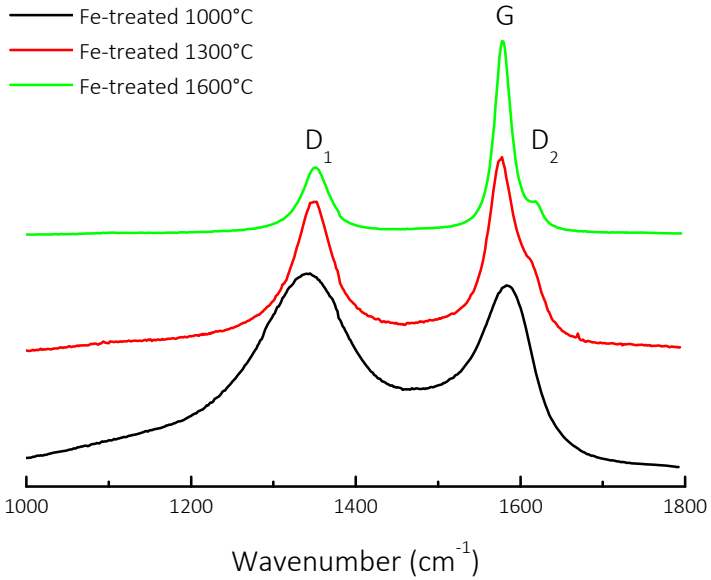
Fe-treated 1000°C
Fe-treated 1300°C
Fe-treated 1600°C
G
D1
D2
1000
1200
1400
1600
1800
Wavenumber (cm-1)

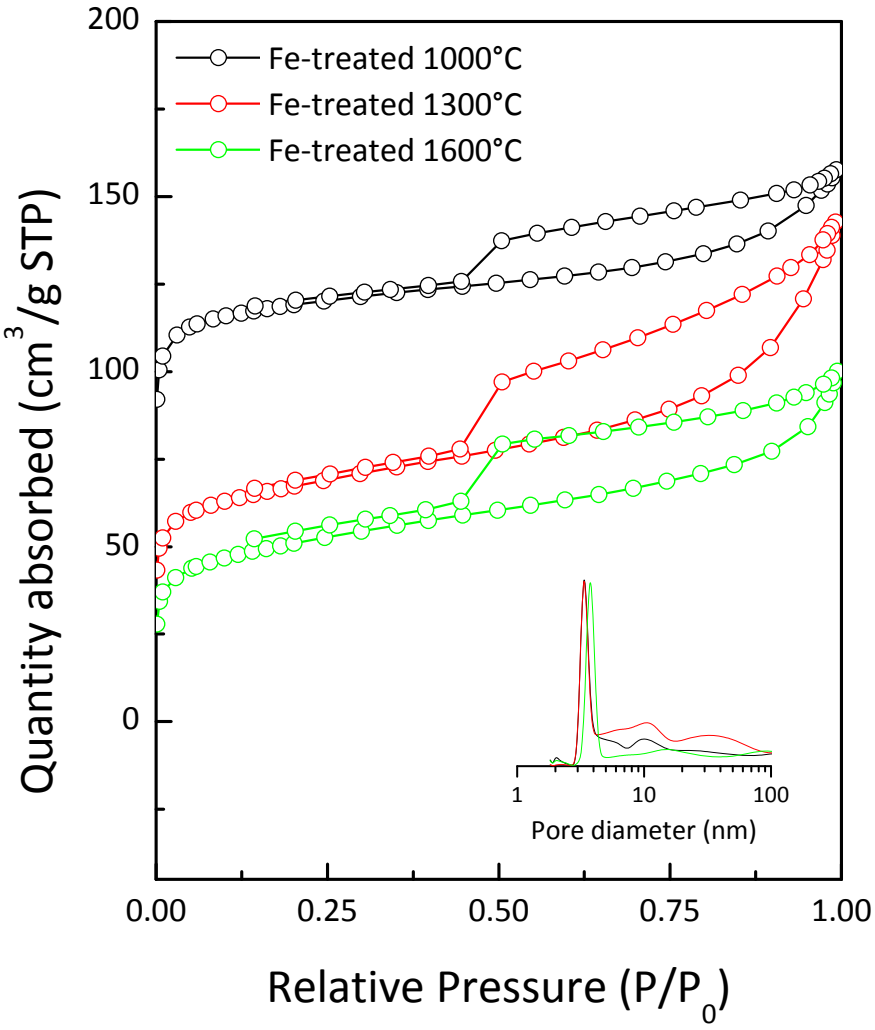
Fe-treated 1000°C
Fe-treated 1300°C
Fe-treated 1600°C
Quantity absorbed (cm3/g STP)
Relative Pressure (P/P0)
200
150
100
50
0
0.00
0.25
0.50
0.75
1.00
1
10
100
Pore diameter (nm)

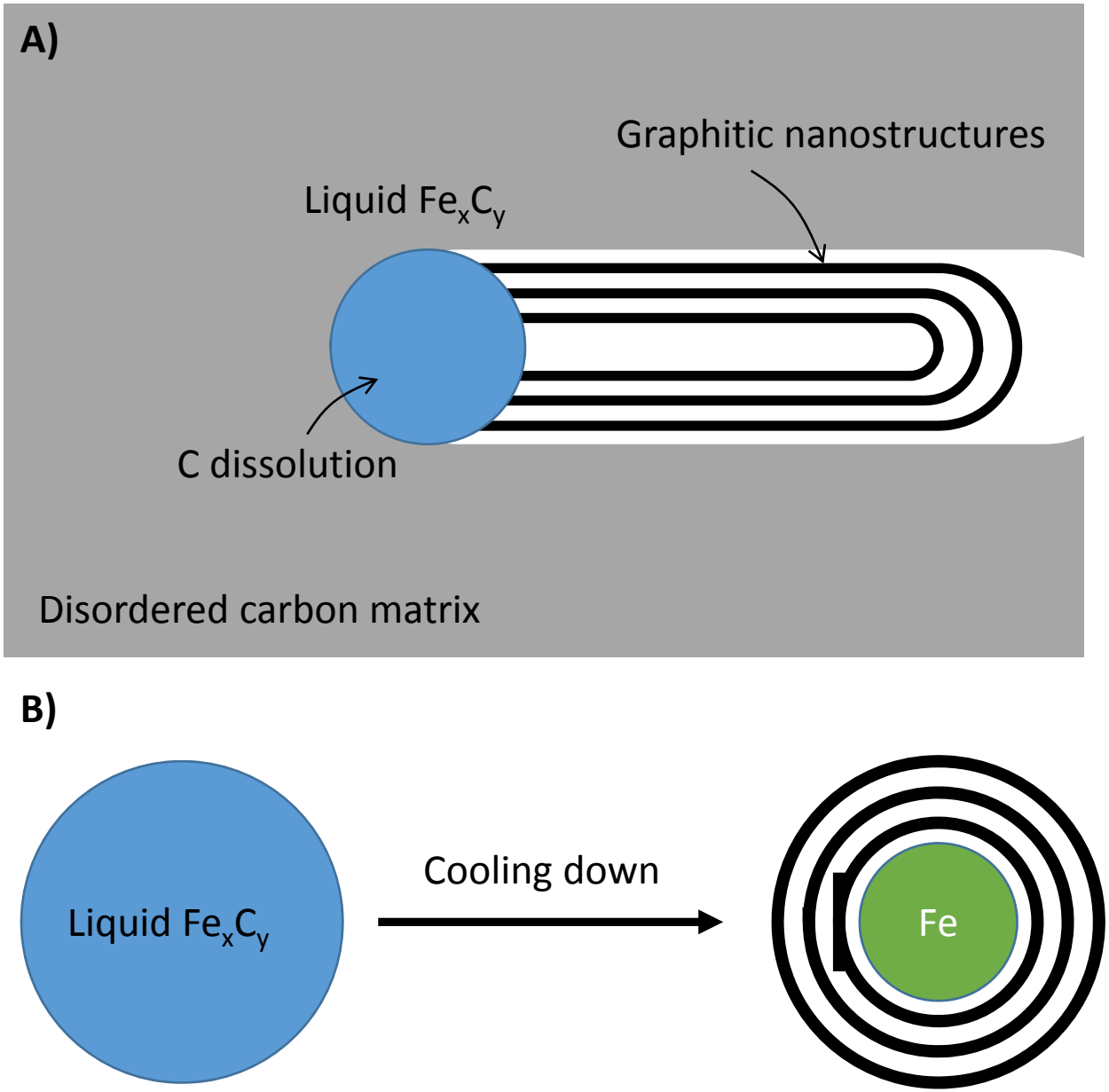
A)
Graphitic nanostructures
Liquid Fe_xC_y
C dissolution
Disordered carbon matrix
B)
Liquid Fe_xC_y
Cooling down
Fe

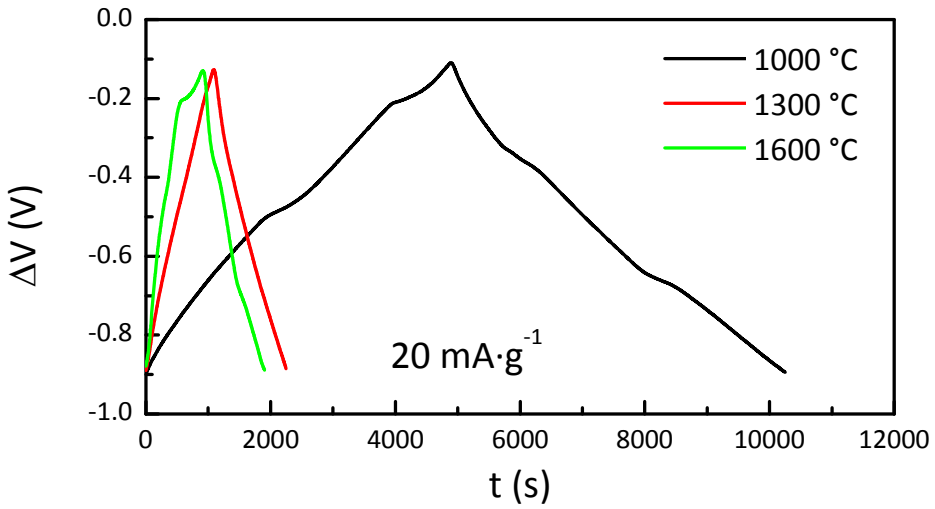
0.0
-0.2
-0.4
-0.6
-0.8
-1.0
ΔV (V)
0
2000
4000
6000
8000
10000
12000
t (s)
1000 °C
1300 °C
1600 °C
20 mA·g-1

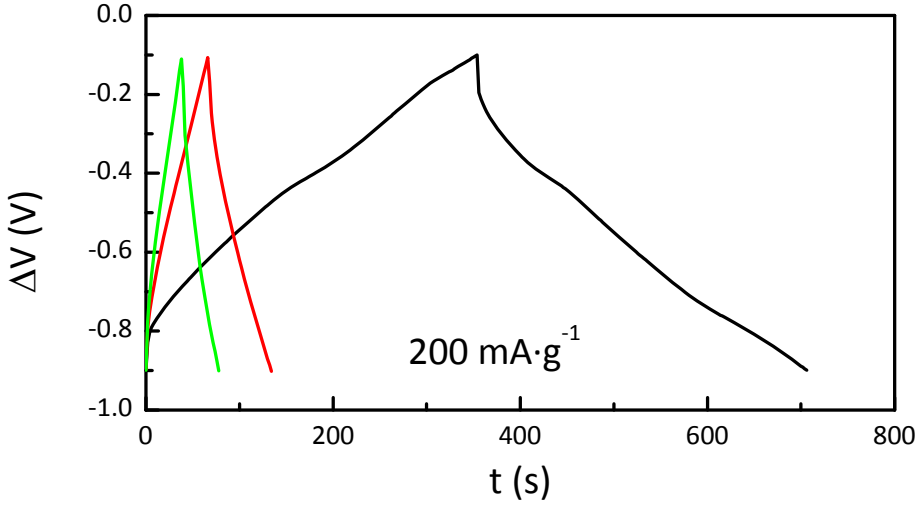
0.0
-0.2
-0.4
-0.6
-0.8
-1.0
ΔV (V)
0
200
400
600
800
t (s)
200 mA·g-1

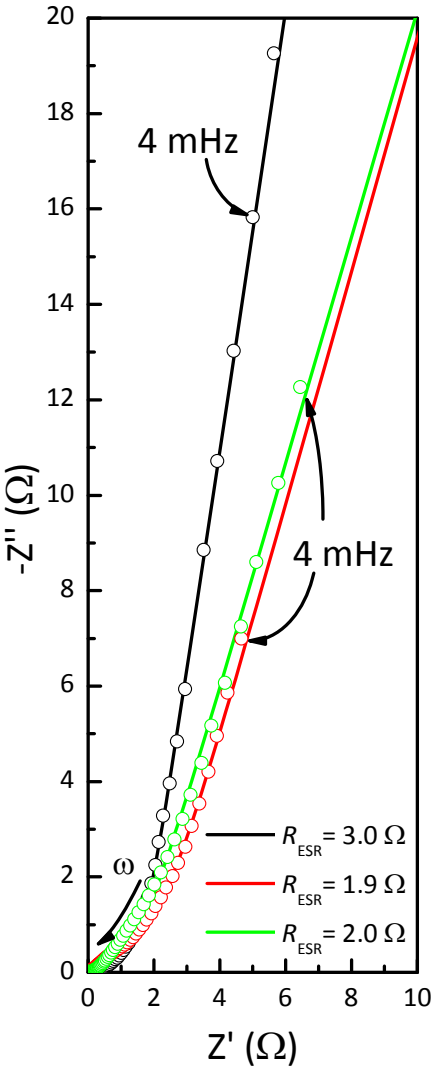
20
18
16
14
12
10
8
6
4
2
0
-Z'' (Ω)
0
2
4
6
8
10
Z' (Ω)
4 mHz
4 mHz
ω
R ESR = 3.0 Ω
R ESR = 1.9 Ω
R ESR = 2.0 Ω

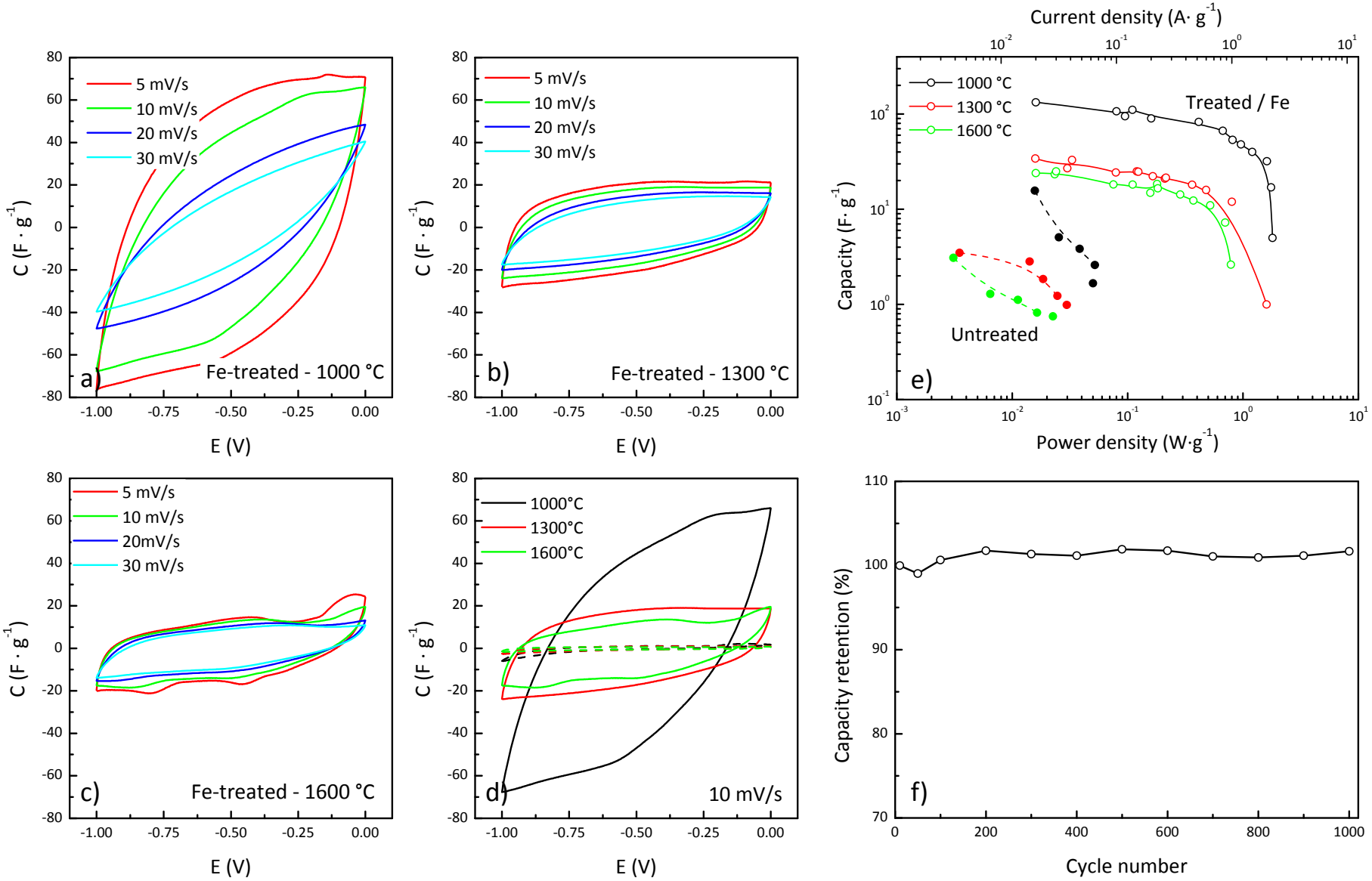
a)
5 mV/s
10 mV/s
20 mV/s
30 mV/s
Fe-treated - 1000 °C
C (F · g-1)
E (V)
b)
5 mV/s
10 mV/s
20 mV/s
30 mV/s
Fe-treated - 1300 °C
C (F · g-1)
E (V)
e)
Current density (A· g-1)
1000 °C
1300 °C
1600 °C
Treated / Fe
Untreated
Capacity (F· g-1)
Power density (W·g-1)
c)
5 mV/s
10 mV/s
20mV/s
30 mV/s
Fe-treated - 1600 °C
C (F · g-1)
E (V)
d)
1000°C
1300°C
1600°C
10 mV/s
C (F · g-1)
E (V)
f)
Capacity retention (%)
Cycle number